# In-line viscosity identification via thermal-rheological measurements in an annular duct for polymer processing

Qiao Lin, Nadine Allanic, Rémi Deterre, Pierre Mousseau, Manuel Girault

# In-line viscosity identification via thermal-rheological measurements in an annular duct for polymer processing

Qiao Lin[a,*], Nadine Allanic[a], Rémi Deterre[a], Pierre Mousseau[a], Manuel Girault[b]

[a] Université de Nantes, Oniris, CNRS, GEPEA, UMR 6144 F-44000 Nantes, France
[b] Institut P' CNRS-ENSMA-Université de Poitiers, UPR 3346, Département Fluides, Thermique, Combustion. ENSMA - Téléport 2. 1 avenue Clément Ader, BP 40109, F86961 Futuroscope Chasseneuil Cedex, France

ARTICLE INFO

*Article history:*
Received 15 July 2021
Revised 3 September 2021
Accepted 18 September 2021
Available online 30 September 2021

*Keywords:*
In-line
Pseudo-plastic
Viscosity
Inverse method
Annular flow
Power law

ABSTRACT

In-line/on-line characterization is more and more important for more flexible and reactive production during the polymer processing. Conventional duct geometries have some disadvantages in terms of measurement efficiency. In this work, several strategies for inverse method are proposed to estimate the viscosity during an injection process via thermal-rheological measurements in an annular duct, which can be positioned downstream of the screw and combined with an axisymmetric model for further in-line monitoring application. The central axis of an annular duct provides sensitive and robust thermal measurements, which can be correlated to the viscosity of the fluid. By analyzing the viscous heating, the heat convection and the pressure loss, the viscosity curve of a power-law fluid can be identified. The identification, involving thermal measurements, can be unsusceptible to the non-homogeneous inlet temperature profile caused by the screw. And the main advantage of these strategies is that the flowrate doesn't necessarily need to be modulated for the identification. That allows in-line viscosity estimation with a poorly known inlet temperature without interfering the production cadence.



## 1. Introduction

In the field of plastic processing, digital simulation's contribution to process analysis and optimization, mold design and production quality improvement is well established [1,2]. While the modeling of polymer flow in the mold runners is an essential step, a good knowledge of the material's thermo-rheological properties (especially the viscosity [3]) is necessary to make the numerical prediction reliable. Some software packages are equipped with databases covering most commonly used polymers' characteristics. However, these may prove to be insufficient and will be all the more so as the rate of recycled and bio-sourced materials with fluctuating and poorly understood characteristics will increase due to current regulatory developments and constraints. The material's viscosity can be measured in the laboratory, under conditions close to process (pressure, shear rate, temperature), in particular by capillary rheometry. Access to this type of equipment, however, remains a hindrance for the industrialist. In addition, the limits of representativeness of this technology (mixing, material heating, experiment duration, etc.) are met for easily degradable [4] or heterogeneous [5] materials. In-line/on-line viscosity measurements are needed to make production more flexible and responsive to the condition of raw materials especially for the next generation materials (In-line analysis occurs directly in the process flow. On-line one takes place when the production is paused or on a side stream channel with an additional pump [6]).

Currently, the most common measurements on a polymer production line are pressure and temperature measurements. In some recent studies, Aho and Syrjälä [7] used a device with a slit die for the on-line injection characterization in 2011. The same type of device (slit die) was used by Zhang and Gilchrist [8] in 2012 to study the microinjection process, by Fernandez & al. [9] in 2014 on recycled polymers and by Mazzanti and Mollica [10] in 2015 on wood plastic composite. In 2019, Luger and Miethlinger [11] used two slit dies of different sizes to obtain two apparent viscosity results, which allow the identification of a two-parameter rheological behavior law (power law [12,13]) without obligation of interfering the flowrate of an extrusion process. Besides, the authors exploited the converging part between the two slit dies to estimate the extensional viscosity. The company named Göttfert has marketed on-line rheometers in extrusion process, for example the BPR capillary rheometer (By-Pass Rheograph), which showed up for the first time in 1986 [14]. Nowadays, their on-line rheometers can be equipped with gear pumps and temperature control system to extract the plastic melt from a production line, characterize the

* Corresponding Author.
*E-mail address:* qiao.lin@univ-nantes.fr (Q. Lin).

**List of symbols**

*Greek letters*

| | |
|---|---|
| $\dot{\gamma}$ | Shear rate ($s^{-1}$) |
| $\overline{\dot{\gamma}}$ | Generalized shear rate ($s^{-1}$) |
| $\overline{\dot{\gamma}}_c$ | Critical shear rate ($s^{-1}$) |
| $\Gamma$ | Boundary |
| $\eta$ | Viscosity (Pa.s) |
| $\lambda$ | Ratio between the zero shear rate (maximum velocity) position the outer radius of an annular flow |
| $\rho_f$ | Flow density ($kg.m^{-3}$) |
| $\rho_s$ | Solid density ($kg.m^{-3}$) |
| $\sigma$ | Ratio between the inner and the outer radius of an annular flow |
| $\tau$ | Shear stress (MPa) |
| $\phi_v$ | Viscous dissipation power ($W.m^{-3}$) |
| $\Omega$ | Domain |

*Latin letters*

| | |
|---|---|
| $C_{p,f}$ | Isobar specific heat capacity of the flow ($J.kg^{-1}.K^{-1}$) |
| $C_{p,s}$ | Isobar specific heat capacity of the solid ($J.kg^{-1}.K^{-1}$) |
| $e$ | Channel thickness (mm) |
| $J_c$ | Cost function of convection ($K^2$) |
| $J_{c+v}$ | Cost function of convection with viscous dissipation ($K^2$) |
| $J_{c+v,p}$ | Weighted dimensionless cost function of convection with viscous dissipation when taking the pressure loss measurement into account |
| $J_p$ | Cost function of pressure loss ($Pa^2$) |
| $J_v$ | Cost function of viscous dissipation ($K^2$) |
| $k_f$ | Thermal conductivity of the flow ($W.m^{-1}.K^{-1}$) |
| $k_s$ | Thermal conductivity of the solid ($W.m^{-1}.K^{-1}$) |
| $K$ | Consistency coefficient of the power law ($Pa.s^n$) |
| $L$ | Length of the annular part in the duct (mm) |
| $L'$ | Distance between the entrance and the annular part in the duct (mm) |
| $n$ | Power-law index |
| $N_{Th}$ | Number of the thermocouples |
| $N_t$ | Number of registered instants |
| $p$ | Pressure (Pa) |
| $Q$ | Flowrate ($cc.s^{-1}$) |
| $R$ | Outer radius of the annular flow (mm) |
| $t$ | Time (s) |
| $t_0$ | Initial time value (s) |
| $t_f$ | Upper time limit (s) |
| $T$ | Temperature (K) |
| $T_i$ | Temperature measured by the thermocouple number $i$ (K) |
| $T_{i,j}$ | Temperature measured by the thermocouple number $i$ at instant $j$ (K) |
| $u$ | Velocity ($m.s^{-1}$) |
| $u_z$ | Velocity projected on the z axis ($m.s^{-1}$) |
| $\bar{u}_z$ | Mean velocity projected on the z axis ($m.s^{-1}$) |

plastic melt with modulated flowrate/temperature and return the plastic melt to the production line afterwards. When using these devices, the estimation of viscosity is mainly achieved via pressure measurements, which often request to modulate the flowrate to obtain a constitutive viscosity law. Most temperature measurements are non-intrusive and easily disturbed by the wall temperature of the tool.

Some studies have revealed the interest and the difficulty to access to the polymer flow's thermal measurements for in-line/on-line monitoring. Karkri & al. [15] developed a slit die equipped

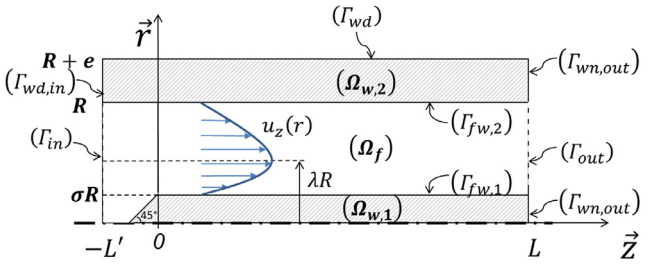


**Fig. 1.** Illustration of the annular flow problem.

with pressure sensors and thermocouples on the die walls. With the pressure and temperature measurements thanks to this device, Pujos & al. [16] proposed an inverse method to identify the rheological behavior law of the material, by using the viscous heating as an information. Assuming that the thermo-rheological properties of the flow are known, the pressure-flow measurements as well as the wall temperature field measured with numerous thermocouples also make it possible to determine, by the inverse method, the temperature profiles at the flow's inlet and outlet [15,17]. However, Karkri & al.'s entire system with the sensors is sizeable and generates high thermal loss. The device is limited to low shear rates and the thermal flow is mainly driven by conduction loss instead of viscous dissipation. Later, Wielhorski & al. [18] designed a cylindrical duct which is capable of working under extrusion and injection conditions, but their device generates too large pressure drops to be positioned in-line. An average temperature as a function of time at the flow's inlet can be estimated by the inverse method with a transient model and the viscous heating taken into account. This device encountered the same difficulty: thermal loss at the die wall where the thermocouples are installed. To overcome this limitation, Launay & al. [19] developed an instrumented cell which can be inserted into a cylindrical duct and measure directly the temperature profile as a function of radius on the section perpendicular to the flow direction. The authors pointed out that the effect of viscous heating can be observed through direct measurement with the cell and that these temperature measurements can be taken into account to supplement standard viscosity (flowrate-pressure) measurements in order to increase the estimated viscosity's accuracy. The disadvantage of the Launay & al.'s device lies in the rheological and thermal disturbances due to the intrusive structure. In order to be able to use a simple cylindrical model to calculate/simulate the flow, without the need to integrate the complex and non-axisymmetric geometry of the cell, corrections to the measurements are necessary to compensate for the intrusive effects of the cell.

To overcome those difficulties, we propose in this paper to study an annular duct, which allows measurements in the heart of the flow while conserving the axisymmetric geometry [20]. A numerical model is presented in the first part of the paper. Then, some analysis on the viscous heating, the heat convection and the pressure loss is performed to demonstrate the correlation between these physical phenomena and the flow's viscosity. Several new strategies of viscosity estimation are discussed. At the end of the paper, an example of inverse identification of a viscosity law is given by using one of the strategies.

## 2. Description of the annular model

An annular axial laminar flow problem can be described as shown in Fig. 1 in an axisymmetric cylindrical coordinate system. The domain $\Omega_{w,1}$ represents the central axis. The domain $\Omega_{w,2}$ represents the channel with $e$ as the outer wall thickness and $L$ as the length of the annular part. The polymer (domain $\Omega_f$) en-

ters the duct at $z = -L'$ and is guided to the annular part by a 45° cone. When $z \geq 0$, the polymer flows between the outer radius $R$ and the inner radius $\sigma R$. $\lambda R$ is the zero shear rate (maximum velocity) position in the radial direction.

It is possible to describe the problem only for $z \geq 0$. Nevertheless, by modeling the cone on the upstream side, we can avoid arbitrary assumption on the thermal boundary condition at the central axis for $z = 0$.

We consider that the flow domain $(\Omega_f)$ is incompressible [21] and at mechanical steady state. Without taking into account the variation in density, the equation of continuity is written as Eq. (1),

$$\mathrm{div}(\vec{u}) = 0 \tag{1}$$

where $\vec{u}$ is the velocity vector. At steady state, the equilibrium equation is written as Eq. (2) when the inertial terms can be neglected compared to the viscous stress [21],

$$0 = -\overrightarrow{\mathrm{grad}}\, p + \overrightarrow{\mathrm{div}}\left(\bar{\bar{\tau}}\right) \tag{2}$$

with $p$ the pressure and $\bar{\bar{\tau}}$ the viscous stress tensor. The incompressible heat equation with viscous heating term for the flow domain $\Omega_f$ is written as Eq. (3),

$$\rho_f C_{p,f}\left(\frac{\partial T}{\partial t} + \mathrm{div}(T\vec{u})\right) = \mathrm{div}\left(k_f \overrightarrow{\mathrm{grad}} T\right) + \phi_v \tag{3}$$

where $T$ is the temperature, $t$ is time; $\rho_f$, $C_{p,f}$ and $k_f$ are the density, the isobar specific heat capacity and the thermal conductivity of the fluid. $\phi_v$ is the viscous dissipation power and can be calculated with Eq. (4),

$$\phi_v = \eta\dot{\bar{\gamma}}^2 = \frac{\eta}{2}\left(\overline{\overline{\mathrm{grad}}}\left(\vec{u}\right) + \left(\overline{\overline{\mathrm{grad}}}\left(\vec{u}\right)\right)^T\right) : \left(\overline{\overline{\mathrm{grad}}}\left(\vec{u}\right) + \left(\overline{\overline{\mathrm{grad}}}\left(\vec{u}\right)\right)^T\right) \tag{4}$$

with $\eta$ being the viscosity and $\dot{\bar{\gamma}}$ being the generalized shear rate. During a polymer process (e.g. extrusion, injection), the shear rate range is mostly located in the pseudo-plastic zone of viscosity curves [21]. In this zone where the viscosity depends highly on the shear rate, the viscosity variation due to the temperature as well as the Newtonian zone of viscosity curves can be neglected [22,23]. The polymer melt is assumed to be pseudo-plastic following the power law [12,13], shown in Eq. (5),

$$\eta = K\dot{\bar{\gamma}}^{n-1} \tag{5}$$

with $K$ the consistency coefficient and $n$ the power-law index ($0 < n < 1$ for pseudo-plastic materials).

In the solid domains $\Omega_{w,1}$ and $\Omega_{w,2}$, only the heat conduction problem (6) is solved,

$$\rho_s C_{p,s}\frac{\partial T}{\partial t} = \mathrm{div}\left(k_s \overrightarrow{\mathrm{grad}} T\right) \tag{6}$$

where $\rho_s$, $C_{p,s}$ and $k_s$ are the density, the isobar specific heat capacity and the thermal conductivity of the solids.

### 2.1. Boundary and initial conditions

The no-slip condition (7) is applied on the surface $(\Gamma_{fw,1})$ of the central axis and on $(\Gamma_{fw,2})$ inside the channel at radius $R$. The temperature and the heat flux are supposed to be continued across the fluid/solid interfaces.

For $r = R,\ z \in [-L',\ L]$, for $r = \sigma R,\ z \in [0,\ L]$ and for $r = \sigma R + z,\ z \in [-\sigma R,\ 0]$,

$$\vec{u} = \vec{0} \tag{7}$$

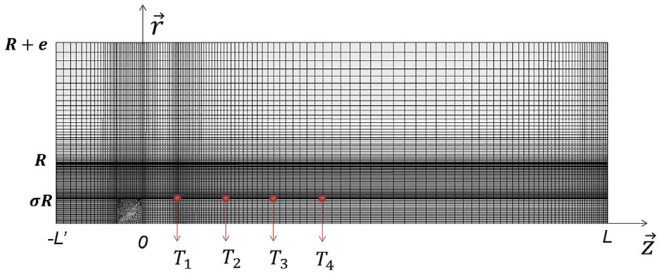


**Fig. 2.** Mesh grid of the numerical simulation.

On the flow inlet $(\Gamma_{in})$, the flowrate (8) and the temperature (9) are fixed.

For $z = -L',\ r \in [0,\ R]$,

$$Q = Q_{in} \tag{8}$$

$$T = T_{in} \tag{9}$$

with $Q_{in}$ and $T_{in}$ the inlet flowrate and the inlet temperature.

On the flow outlet $(\Gamma_{out})$ and the outlet walls $(\Gamma_{wn,out})$, the Neumann condition (10) is applied.

For $z = L,\ r \in [0,\ R + e]$,

$$\frac{\partial T}{\partial z} = 0 \tag{10}$$

On the side wall $(\Gamma_{wd})$ and the inlet wall of the duct $(\Gamma_{wd,in})$, the Dirichlet conditions (11) and (12) are applied. A linear interpolation between the temperatures $T_w$ and $T_{in}$ is used on $(\Gamma_{wd,in})$ to ensure the continuity of the temperature field.

For $r = R + e,\ z \in [-L',\ L]$,

For $z = -L',\ r \in [R,\ R + e]$,

$$T = T_w \tag{11}$$

$$T = \frac{T_w - T_{in}}{e}(r - R) + T_{in} \tag{12}$$

The velocity field is established instantly when $t > 0$ s and doesn't vary with respect to $t$. The average temperature of system equals $T_w$ at $t = 0$ s.

### 2.2. Numerical method and parameters

The software « ANSYS® POLYFLOW® » is used to simulate our axisymmetric model. The mesh grid, presented in Fig. 2, is composed by 16218 nodes and 15946 linear quadrilateral elements. The sizes of the elements are less than 2 mm and refined at the intersections of domains or near the section change area of the flow.

Picard iteration [24] and Crank-Nicolson method [25] are used for solving our nonlinear flow equations and thermal transient problem. The initial time step is set to 0.001 s. The largest calculation time step is less than 0.1 s, with an initial time value $t_0 = 0$ s and an upper time limit $t_f = 2$ s to simulate a short injection sequence.

The geometric parameters are chosen according to the flow dimensions commonly used on a polymer production line: $L = 76$ mm, $L' = 14$ mm, $e = 20$ mm, $R = 10$ mm and $\sigma = 0.4$. The material of the solid domains $(\Omega_{w,1})$ and $(\Omega_{w,2})$ is stainless steel with a thermal conductivity of 15 $\mathrm{W.m^{-1}.K^{-1}}$, a density of 7900 $\mathrm{kg.m^{-3}}$ and a specific heat capacity of 500 $\mathrm{J.kg^{-1}.K^{-1}}$. The properties of Polypropylene are used as reference ones for the polymer flow domain $\Omega_f$ with a thermal conductivity of 0.23 $\mathrm{W.m^{-1}.K^{-1}}$, a density of 900 $\mathrm{kg.m^{-3}}$ and a specific heat capacity of 2800 $\mathrm{J.kg^{-1}.K^{-1}}$.

The temperature $T_{in}$ and $T_w$ are set to 473.15 K and the flowrate $Q_{in}$ is 30 $\mathrm{cc.s^{-1}}$ (mean velocity $\bar{u}_z = 0.11$ $\mathrm{m.s^{-1}}$ in the annular

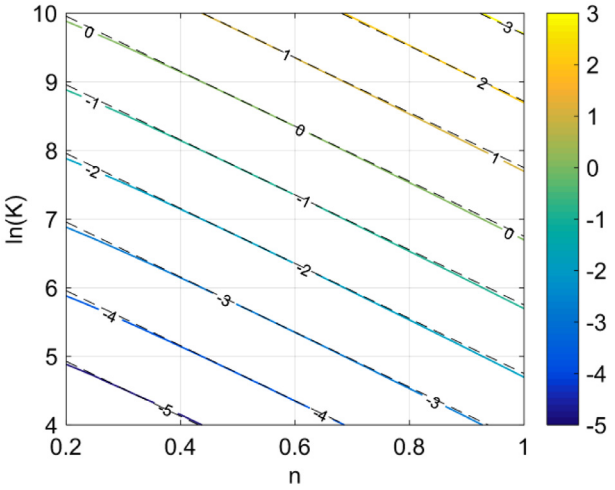


**Fig. 3.** Isolines of ln $[T_4(t_f) - T_4(t_0)]$ temperature variation caused by the viscous heating at the thermocouple N°4 after 2 seconds of injection with a flowrate of 30 cc.s$^{-1}$ compared to dashed straight lines with a slope of 0.401.

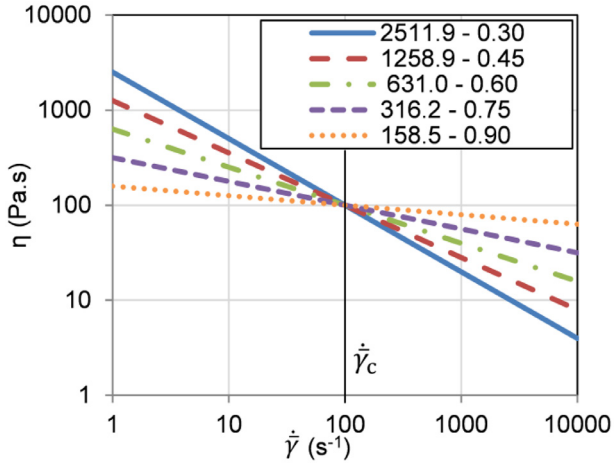


**Fig. 4.** Example of power laws passing through the common point $[\dot{\bar{\gamma}}_c = 100\ s^{-1}, \eta_c = 100\ Pa.s]$ with parameters *K*-*n* for *K* varying from 2511.9 to 158.5 Pa.s$^n$ and *n* varying from 0.3 to 0.9.

part) in the first place for injection simulation. The Graetz number in the annular part $[\rho_f C_{p,f} \bar{u}_z (R-\sigma R)^2/(k_f L)]$ reaches 590, which means that the radial heat conduction in the flow is insignificant compared to the axial heat advection. It's difficult for an external thermal perturbation to travel in the radial direction across the flow to reach the central axis. In the software « ANSYS® POLYFLOW® », four virtual thermocouples $T_i$ with $i = 1, 2, 3, 4$ are installed on the central axis' wall at $[r = \sigma R]$ from $z = 6$ mm to $z = 34$ mm with equidistance between them (Fig. 2). Thanks to the large Graetz number, the polymer flow around the central axis can render these measurements unsusceptible to external thermal disturbance at $[R \le r \le R + e]$.

## 3. Correlation analysis between the thermo-rheological phenomena and the viscosity parameters

Simulations are carried out with the presented model to study the correlation of our measurements in a thermally transient state with respect to the *K* and *n* parameters of the power law (5). *n* varies from 0.2 to 1 with a step of 0.025 and ln(*K*) varies from 4 to 10 with a step of 0.1875 (*K* varies from 54.6 to 22 026.5 Pa.s$^n$).

### 3.1. Viscous heating

In the annular part where the velocity profile is stabilized, the viscous dissipation can be written as Eq. (13) obtained from the shear rate, the power-law and the flowrate equations in [26], with parameters given in Fig. 1 and *Q* as the flowrate.

$$\phi_v = K\left[\frac{Q(3n+1)}{\pi n R^3\left[\left(1-\lambda^2\right)^{\frac{1}{n}+1} - \sigma^{1-\frac{1}{n}}\left(\lambda^2-\sigma^2\right)^{\frac{1}{n}+1}\right]}\right]^{n+1} \left|\lambda^2\left(\frac{r}{R}\right)^{-1} - \frac{r}{R}\right|^{\frac{1}{n}+1} \tag{13}$$

$\lambda$ depends on the power-law parameter *n* and the geometry parameter $\sigma$ [26]. It should be noted that the viscous dissipation (Eq. (13)), which is related to the viscosity, has its maximal value on the central axis wall $[r = \sigma R]$. Therefore, the central axis is more sensitive to this thermal phenomenon, which can be used to identify the material's viscosity law [16].

In Fig. 3, the increase in temperature due to viscous dissipation at thermocouple N°4 $[r = \sigma R,\ z = 34$ mm$]$ after 2 seconds of injection compared to the initial state: $[T_4(t_f) - T_4(t_0)]$, is presented on a natural logarithm scale as a function of ln(*K*) and *n*. The isovalues of ln $[T_4(t_f) - T_4(t_0)]$ are drawn with solid lines. Several dashed straight lines with a slope of 0.401 are also plotted on the same figure.

The isotemperature lines in Fig. 3 are close to those straight dashed lines, which means that the parameters $(n, \ln(K))$ of the materials giving the same thermal response $[T_4(t_f) - T_4(t_0)]$ are close to be on a straight line $[\ln(K) = An + B]$. In fact, the representative surface of Fig. 3 is close to a plane with a Pearson product-moment correlation coefficient [27] of 99.991%.

This phenomenon is also observed on thermocouples number 1 to 3 for other injection times. Indeed, the power law (5) can also be written on a logarithmic scale: $[\ln(\eta) = \ln(K) + (n+1)\ln(\dot{\bar{\gamma}})]$. If a set of materials, having different viscosity curves $\eta(\dot{\bar{\gamma}})$, share a common point $(\dot{\bar{\gamma}}_c, \eta_c)$ as the example in Fig. 4, the parameters $(n, \ln(K))$ of these materials follow the linear relation (14).

$$\ln(K) = -\ln\left(\dot{\bar{\gamma}}_c\right)n + \ln(\eta_c) + \ln\left(\dot{\bar{\gamma}}_c\right) \tag{14}$$

In other words, for this inverse method strategy, although there can be infinity of combinations *K*-*n* which give the same temperature $T_i$ measured by a thermocouple at an instant *t*, we can confirm a zone around a point $(\dot{\bar{\gamma}}_c, \eta_c)$ on the desired viscosity law, because the latter is among the curves passing through the common zone. As in conical indentation [28], we just need two different points to identify a constitutive law which has two parameters (Fig. 5). It is also possible to draw a law without being based on an existing model, from a point cloud obtained with the power-law approach.

To apply the strategy, one possible way to calculate $\dot{\bar{\gamma}}_c$ is using the slope of the line described by Eq. (14) which can be obtained by an interpolation (in Fig. 3) for example from all points $(n, \ln(K))$ having the same isovalue $[T_i(t) - T_i(t_0)]$, for each thermocouple at each instant *t*. By exploiting the simulation results around a reference coordinate: $n = 0.6$ and $\ln(K) = 7$, it is confirmed that each flowrate, each thermocouple and each instant *t* gives a different point $(\dot{\bar{\gamma}}_c, \eta_c)$. The values of $\dot{\bar{\gamma}}_c$ are shown in table 1.

It should be noted that the critical shear rate $\dot{\bar{\gamma}}_c$ does not represent the shear rate on the surface of the central axis. The value of $\dot{\bar{\gamma}}_c$ in table 1 is more sensitive to the flowrate's variation compared to the other parameters (thermocouple's location, injection time). At a sufficiently large instant *t* (for example $t = 2$ s), $\dot{\bar{\gamma}}_c$ varies almost linearly with respect to the flowrate. That is to say,

**Table 1**
$|\dot{\bar{\gamma}}_c|$ depending on flowrate, thermocouple and time.

| $\dot{\bar{\gamma}}_c$ in $s^{-1}$ for a flowrate of 30 $cc.s^{-1}$ | | | | |
|---|---|---|---|---|
| | $t = 0.5$ s | $t = 1$ s | $t = 1.5$ s | $t = 2$ s |
| Thermocouple 1 | 51.73 | 55.10 | 56.36 | 57.25 |
| Thermocouple 2 | 45.37 | 52.63 | 54.48 | 55.60 |
| Thermocouple 3 | 43.34 | 51.50 | 54.01 | 55.31 |
| Thermocouple 4 | 42.79 | 50.04 | 53.65 | 55.16 |
| $\dot{\bar{\gamma}}_c$ in $s^{-1}$ for a flowrate of 60 $cc.s^{-1}$ | | | | |
| | $t = 0.5$ s | $t = 1$ s | $t = 1.5$ s | $t = 2$ s |
| Thermocouple 1 | 106.02 | 110.69 | 112.92 | 114.63 |
| Thermocouple 2 | 99.52 | 106.60 | 109.38 | 111.28 |
| Thermocouple 3 | 94.24 | 105.38 | 108.66 | 110.67 |
| Thermocouple 4 | 90.18 | 104.60 | 108.30 | 110.47 |
| $\dot{\bar{\gamma}}_c$ in $s^{-1}$ for a flowrate of 90 $cc.s^{-1}$ | | | | |
| | $t = 0.5$ s | $t = 1$ s | $t = 1.5$ s | $t = 2$ s |
| Thermocouple 1 | 160.32 | 166.23 | 169.53 | 172.26 |
| Thermocouple 2 | 152.50 | 160.38 | 164.23 | 167.04 |
| Thermocouple 3 | 148.64 | 159.10 | 163.23 | 166.02 |
| Thermocouple 4 | 143.59 | 158.07 | 162.73 | 165.65 |

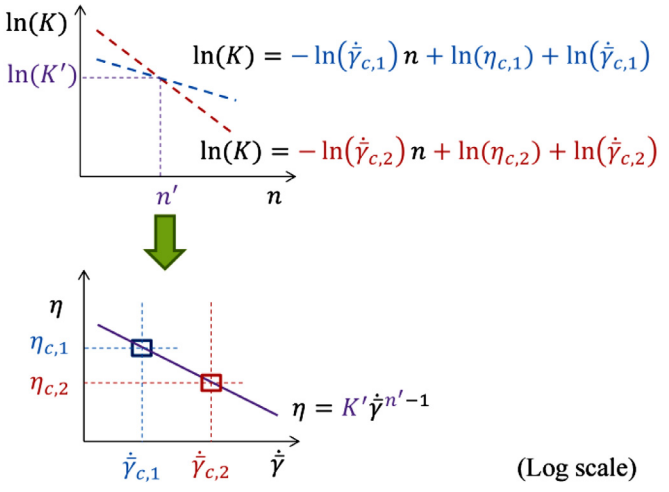


**Fig. 5.** Inverse method strategy by using $(\dot{\bar{\gamma}}_c, \eta_c)$ points obtained from the viscous dissipation analysis.

by varying the flowrate, several points $(\dot{\bar{\gamma}}_c,\eta_c)$ as well as a viscosity law can be identified.

For example, after three injections of 2 seconds, at a flowrate of 30 $cc.s^{-1}$, 60 $cc.s^{-1}$ and 90 $cc.s^{-1}$, the thermocouple N°4 measures respectively a temperature variation of $e^{0.85} = 2.3$ K, $e^{1.68} = 5.4$ K and $e^{2.15} = 8.6$ K. We can draw, in Fig. 6a, three isotemperature lines. The common points of these lines are close to $\ln(K) = 9.798$ ($K = 18000$ Pa.s$^n$) and $n = 0.45$, which are indeed the parameters (PE [29]) used in a simulation to obtain the mentioned temperature measurements for those three injections.

In practice, we can obtain the expression of a straight line (Eq. (14)) fitting each isotemperature line from at least two random points on the isotemperature line. Knowing that the expressions of the straight lines are $[\ln(K) = -4.01n + 11.601]$ for a flowrate of 30 $cc.s^{-1}$, $[\ln(K) = -4.70n + 11.912]$ for a flowrate of 60 $cc.s^{-1}$ and $[\ln(K) = -5.11n + 12.098]$ for a flowrate of 90 $cc.s^{-1}$, we can calculate three critical points thanks to Eq. (14): $[\dot{\bar{\gamma}}_{c,1} = 55.16\ s^{-1}, \eta_{c,1} = 1979.82$ Pa.s] for a flowrate of 30 $cc.s^{-1}$; $[\gamma_{c,2} = 110.47\ s^{-1}, \eta_{c,2} = 1349.19$ Pa.s] for a flowrate of 60 $cc.s^{-1}$ and $[\gamma_{c,3} = 55.16\ s^{-1}, \eta_{c,3} = 1083.69$ Pa.s] for a flowrate of 90 $cc.s^{-1}$. These critical points are plotted in Fig. 6b with a power law drawn for $K = 18000$ Pa.s$^n$ and $n = 0.45$. By linear regression using these critical points, a power law can be thus identified with $K = 17847$ Pa.s$^n$ and $n = 0.4515$ (Fig. 6b).

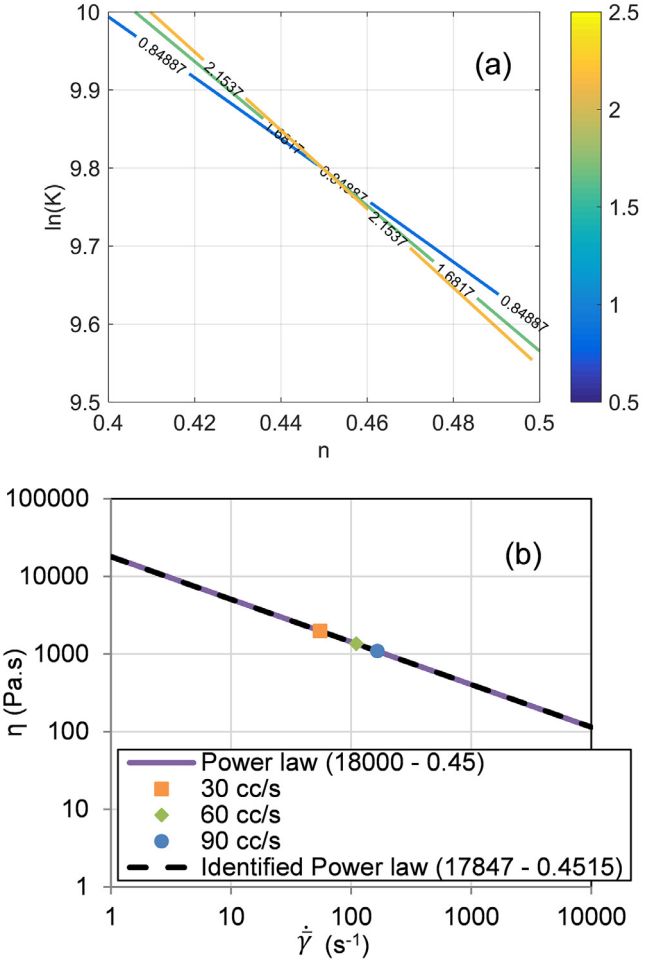


**Fig. 6.** Example of viscosity estimation via viscous dissipation: (a) Isolines of $\ln[T_4(t_f) - T_4(t_0)]$ at the value of 0.85, 1.68 and 2.15 for a flowrate of 30 $cc.s^{-1}$, 60 $cc.s^{-1}$ and 90 $cc.s^{-1}$ (b) viscosity law for $K = 18000$ Pa.s$^n$ and $n = 0.45$ with three critical points and the identified power law for $K = 17847$ Pa.s$^n$ and $n = 0.4515$.

However, conventional characterization methods (capillary, Couette, cone-plate rheometer, etc.) already allow obtaining a viscosity law with several different flowrates. At a constant flowrate, the value of $\dot{\bar{\gamma}}_c$ in table 1 varies slightly depending on the time and location of measurement (thermocouple). It would perhaps be pos-

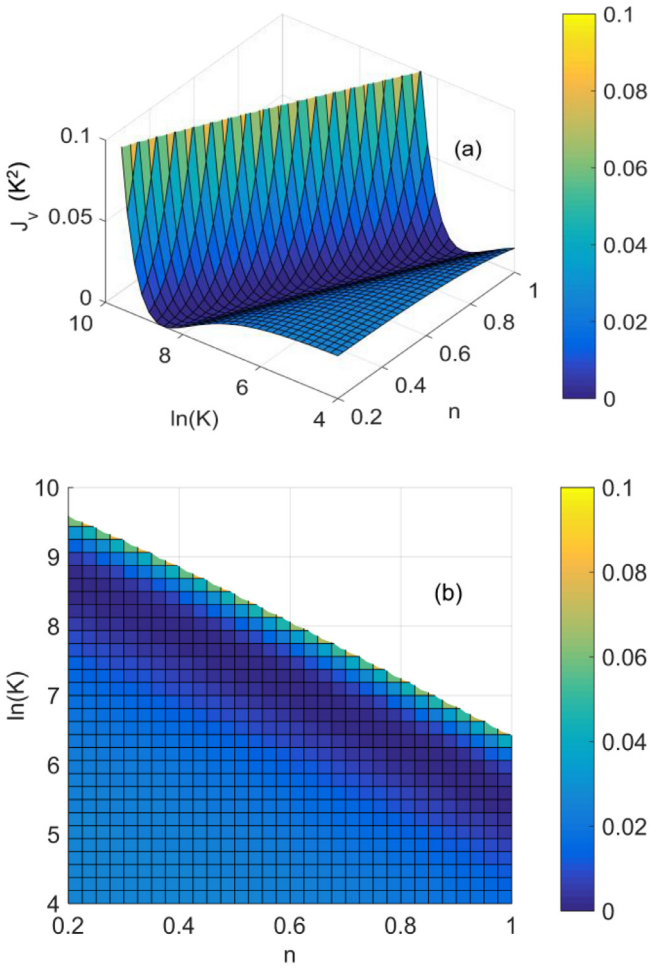


**Fig. 7.** (a) 3D view and (b) 2D view of $J_v$ as a function of $n$ and $\ln(K)$ with respect to the reference $[n = 0.6, \ln(K) = 7]$ with a flowrate of 30 cc.s$^{-1}$.

sible, with a single flowrate (30 cc.s$^{-1}$), to identify an entire power law by taking into account all the measurements (for all the thermocouples and all the instants $t$) in the cost function during the inverse method as in spherical indentation [30]. We define $J_v$ the cost function related to viscous dissipation as shown in Eq. (15),

$$J_v = \frac{\sum_{j=1}^{N_t}\sum_{i=1}^{N_{Th}}\left(T_{i,j} - T^*_{i,j}\right)^2}{N_{Th}N_t} \tag{15}$$

with $N_{Th}$ the number of thermocouples, $N_t$ the number of registered instants, $T_{i,j}$ the temperature and $T^*_{i,j}$ the reference temperature measured by thermocouple number $i$ at time number $j$.

Let us take the thermal responses of a material with $n = 0.6$ and $\ln(K) = 7$ as a reference $T^*_{i,j}$. Fig. 7 shows the image of $J_v$ as a function of $n$ and $\ln(K)$.

A valley of minimum, passing through the point $n = 0.6$ and $\ln(K) = 7$, is observed in Fig. 7. The different combinations $K$-$n$ at the bottom of the valley give very low values of $J_v$, therefore thermal responses $T_{i,j}$ very close to those of the reference $T^*_{i,j}$. The identification of an entire power law can't be ensured by just taking all the thermal measurements into account in the cost function during the viscous heating analysis with a consistent flowrate. Nevertheless, the minimum valley of the cost function $J_v$ can still be used to identify one critical point of the power law for each different flowrate. In practice, the direction of the minimum valley can be calculated with a Hessian matrix during inverse characterization.

### 3.2. Heat convection

Besides viscous dissipation, there is also the convection heat exchange between the flow and the central axis. The efficiency of convection exchange depends not only on thermal properties but also on the velocity profile of the flow. For a power-law (viscosity) fluid at a flowrate $Q$ in an annular geometry, the shear rate profile (16) and (17) can be obtained from the shear rate and the flowrate equations in [26].

For $r \in [\sigma R,\ \lambda R]$,

For $r \in [\lambda R, R]$,

$$\dot{\gamma} = \frac{Q(3n+1)}{\pi n R^{\frac{1+3n}{n}}\left[\left(1-\lambda^2\right)^{\frac{1}{n}+1} - \sigma^{1-\frac{1}{n}}\left(\lambda^2-\sigma^2\right)^{\frac{1}{n}+1}\right]}\left(\frac{\lambda^2R^2}{r} - r\right)^{\frac{1}{n}} \tag{16}$$

$$\dot{\gamma} = -\frac{Q(3n+1)}{\pi n R^{\frac{1+3n}{n}}\left[\left(1-\lambda^2\right)^{\frac{1}{n}+1} - \sigma^{1-\frac{1}{n}}\left(\lambda^2-\sigma^2\right)^{\frac{1}{n}+1}\right]}\left(r - \frac{\lambda^2R^2}{r}\right)^{\frac{1}{n}} \tag{17}$$

Since $\lambda$ depends itself on the power-law parameter $n$ and the geometry parameter $\sigma$ [26], the shear rate depends only on the parameter $n$ when the geometry parameters and the flowrate are fixed. The velocity profile, obtained by integrating shear rate profile, therefore depends only on the parameter $n$.

To study the contribution of convection heat exchange in the viscosity estimation, $T_{in}$ the inlet temperature is increased by 20 K (which is a reasonable temperature variation on a production line [31] without involving the temperature dependence of viscosity for Polypropylene and Polyethylene [32]) in our next simulation with a flowrate at 30 cc.s$^{-1}$. The temperature rise at the central axis will be due to convection and viscous dissipation. We introduce $J_{c+v}$ the cost function related to convection and viscous dissipation as described in Eq. (18),

$$J_{c+v} = \frac{\sum_{j=1}^{N_t}\sum_{i=1}^{N_{Th}}\left(\tilde{T}_{i,j} - \tilde{T}^*_{i,j}\right)^2}{N_{Th}N_t} \tag{18}$$

with $\tilde{T}_{i,j}$ and $\tilde{T}^*_{i,j}$ to differentiate them from $T_{i,j}$ and $T^*_{i,j}$ of Eq. (15).

The thermal responses of a material with $n = 0.6$ and $\ln(K) = 7$ are used as a reference $\tilde{T}^*_{i,j}$. Fig. 8 shows the image of $J_{c+v}$ as a function of $n$ and $\ln(K)$.

In Fig. 8, all values of $J_{c+v}$ at the bottom of the curved minimum valley are close to zero. We can spot a zone where viscous dissipation is dominant. This zone, which represents relatively viscous materials with large values of $K$-$n$, has part of the minimum valley following a direction similar to that of Fig. 7. Regarding relatively fluid materials with low values of $K$-$n$ in the figure, the value of $J_{c+v}$ is insensitive to the parameter $K$. This part of the valley takes the direction almost perpendicular to the $n$ axis in this zone where the materials cannot generate a large viscous dissipation so that the heat exchange by convection is dominant.

To confirm the correlation of the heat exchange by convection with respect to the parameter $n$, we then introduce $J_c$ the cost function related to the convection as shown in Eq. (19).

$$J_c = \frac{\sum_{j=1}^{N_t}\sum_{i=1}^{N_{Th}}\left[\left(\tilde{T}_{i,j} - T_{i,j}\right) - \left(\tilde{T}^*_{i,j} - T^*_{i,j}\right)\right]^2}{N_{Th}N_t} \tag{19}$$

$\tilde{T}_{i,j}$ and $\tilde{T}^*_{i,j}$ are the temperatures of the « convection with viscous dissipation » simulation (Eq. (18)). $T_{i,j}$ and $T^*_{i,j}$ are the temperatures of the « viscous dissipation » simulation (Eq. (15)).

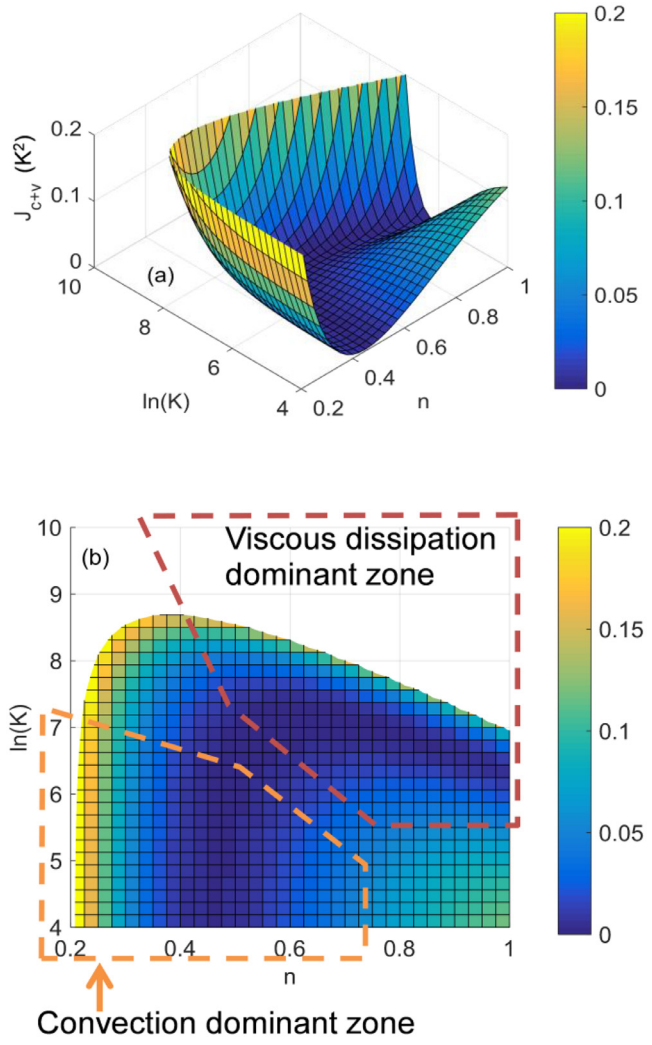


**Fig. 8.** (a) 3D view and (b) 2D view of $J_{c+v}$ as a function of $n$ and $\ln(K)$ with respect to the reference [$n = 0.6, \ln(K) = 7$], with a flowrate of 30 cc.s$^{-1}$.

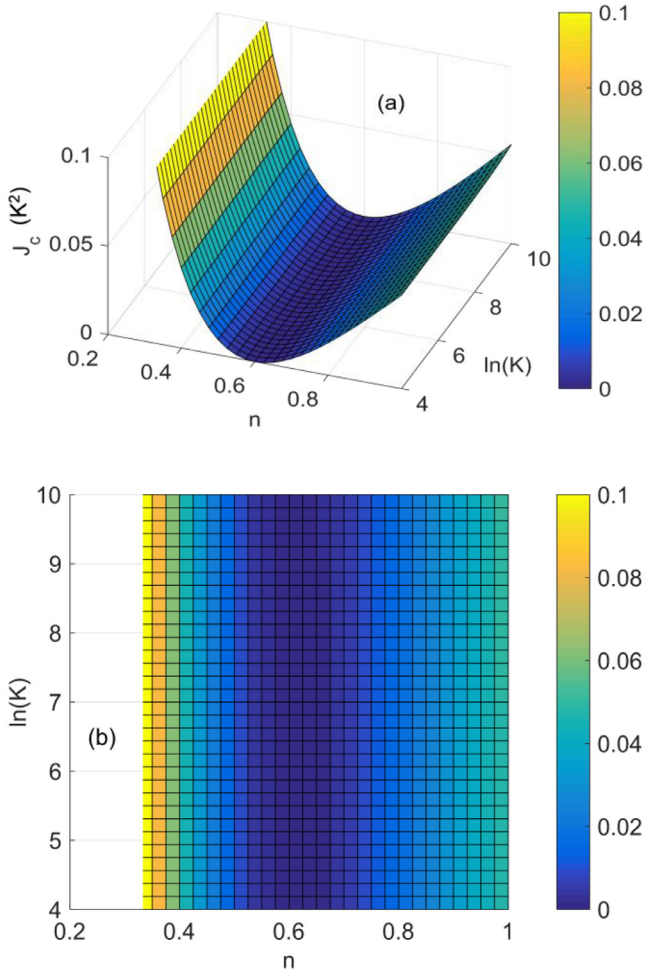


**Fig. 9.** (a) 3D view and (b) 2D view of $J_c$ as a function of $n$ and $\ln(K)$ with respect to the reference [$n = 0.6$, $\ln(K) = 7$], with a flowrate of 30 cc.s$^{-1}$.

Always with respect to the reference $n = 0.6$ and $\ln(K) = 7$, Fig. 9 shows the image of $J_c$ as a function of $n$ and $\ln(K)$.

Fig. 9 confirms that heat exchange by convection is insensitive to the parameter $K$ and depends mainly on the parameter $n$.

Let's define the word: differential convection characterization, which can be achieved by modifying the inlet temperature between two injections to identify the parameter $n$ (Fig. 9). The differential convection characterization can also be performed by applying different initial temperature fields of the central axis to two injections, with the same inlet temperature profile which is supposed to be repeatable on a production line. The latter option allows the characterization without the need of knowing precisely the inlet temperature profiles as long as they are the same during those two injections. This can be considered as an advantage for in-line characterization where the inlet temperature profile is highly non-homogeneous.

We can also imagine an annular device with a central axis which can be heated up (for example by an electric resistance installed inside). This device can have a better control on the initial temperature fields especially at the central axis. The heating central axis opens up another option which is to perform the differential convection characterization by using different heating powers between two injections. The option also removes the need of knowing precisely the inlet temperature profiles, as long as they are the same during those two injections.

### 3.3. Pressure loss

At a constant flowrate $Q$, the pressure loss of a power-law fluid in an annuli can be described as Eq. (20) from the flowrate equation in [26,33].

$$\frac{dp}{dz} = -2K\left[\frac{Q(3n+1)}{\pi n R^{\frac{1+3n}{n}}\left[\left(1-\lambda^2\right)^{\frac{1}{n}+1} - \sigma^{1-\frac{1}{n}}\left(\lambda^2-\sigma^2\right)^{\frac{1}{n}+1}\right]}\right]^n \quad (20)$$

The pressure loss depends linearly on the parameter $K$. Since $\lambda$ can be estimated with methods presented in [26], we can confirm with the analytical Eq. (20) that the isovalue curves of the pressure loss are not straight lines in the $\ln(K) - n$ space. However, they can be close to the minimum valley of the viscous heating cost function $J_v$ (Fig. 7) as shown in Fig. 10 where the pressure loss cost function $J_p$ is written as Eq. (21) with $dp^*/dz$ the reference pressure loss for $n = 0.6$ and $\ln(K) = 7$.

$$J_p = \left(\frac{dp}{dz} - \frac{dp^*}{dz}\right)^2 \quad (21)$$

Consequently, the use of $J_v$ along with $J_p$ may not guarantee the uniqueness of solution during an inverse method.

**Table 2**
Different viscosity estimation strategies.

| Viscosity estimation strategies | Number of injection | Flowrate | Thermal condition | Pressure | Temperature |
|---|---|---|---|---|---|
| Capillary | >1 | Modulated | Fixed | Measured | / |
| $J_v$ | >1 | Modulated | Fixed | / | Measured |
| $J_c + J_v$ | 2 | Fixed | Modulated | / | Measured |
| $J_c + J_p$ | 2 | Fixed | Modulated | Measured | Measured |
| $J_{c+v} + J_p$ | 1 | / | / | Measured | Measured |

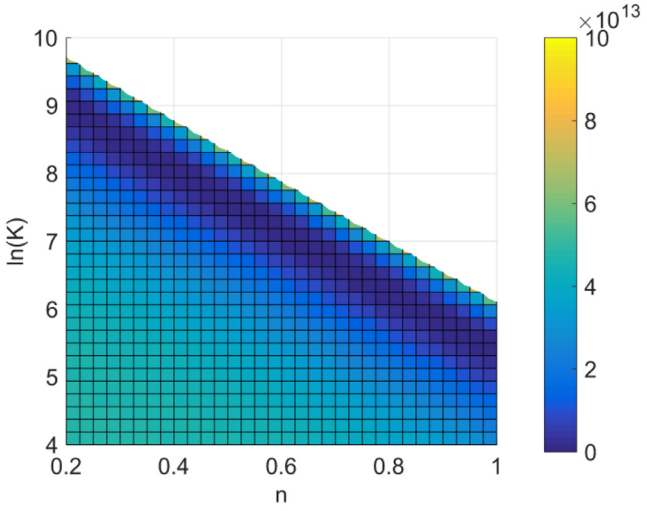


**Fig. 10.** $J_p$ as a function of $n$ and $\ln(K)$ with respect to the reference [$n = 0.6, \ln(K) = 7$], with a flowrate of 30 cc.s$^{-1}$.

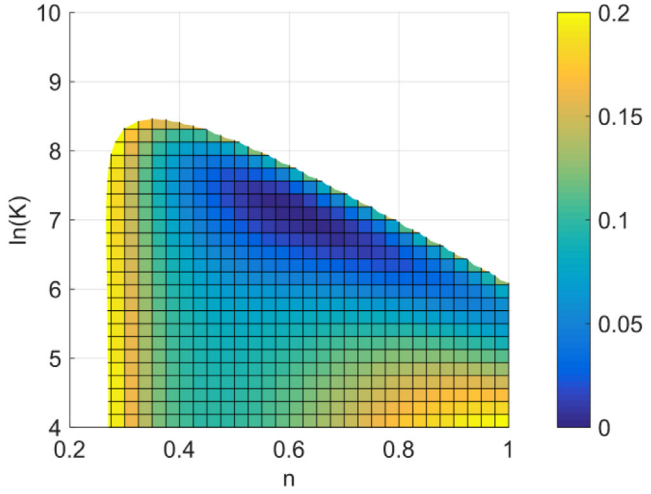


**Fig. 11.** $J_{c+v,p}$ as a function of $n$ and $\ln(K)$ with respect to the reference [$n = 0.6, \ln(K) = 7$], with a flowrate of 30 cc.s$^{-1}$.

## 4. Inverse analysis

A summary of several viscosity estimation strategies is presented in table 2. The conventional capillary viscosity estimation consists in measuring the pressure loss with a modulated flowrate. According to the analysis above, it is possible to obtain a viscosity law via the viscous heating analysis (cost function $J_v$) with a modulated flowrate without the need of applying Rabinowitsch correction [34].

The differential convection characterization mentioned in this paper requires two injections with modulated thermal condition to identify the power-law index $n$. The viscous heating analysis can be carried out during one of those two injections and so as the pressure loss measurement, to obtain a relation between $K$ and $n$. It is hence possible to combine either a pressure loss cost function $J_p$ or a viscous heating cost function $J_v$ with the differential convection characterization cost function $J_c$ to obtain a unique power law curve by inverse method via two injections with a consistent flowrate (table 2).

With only one injection, it is always possible to integrate the pressure loss measurement $J_p$ and the thermal measurement $J_{c+v}$ (Eq. (18), Fig. 8) when the heat convection is dominant enough compared to the viscous heating (table 2). An example with weighting coefficients is given by Eq. (22) using $J_{c+v}$ in Fig. 8 and $J_p$ in Fig. 10,

$$J_{c+v,p} = \alpha \frac{J_{c+v}}{\frac{\sum_{j=1}^{N_t}\sum_{i=1}^{N_{Th}}\left(\tilde{T}^*_{i,j}-\tilde{T}_{i,0}\right)^2}{N_{Th}N_t}} + \beta \frac{J_p}{\left(\frac{dp^*}{dz}\right)^2} \tag{22}$$

with $\alpha = 5$, $\beta = 0.1$ and $\tilde{T}_{i,0}$ the initial temperature at $t = 0$ s measured by the thermocouple number $i$. There are many approaches for making the terms dimensionless in Eq. (22). Here, the term $J_{c+v}$ is divided by the least-square difference of the reference measurements $\tilde{T}^*_{i,j}$ compared to the initial temperature field $\tilde{T}_{i,0}$. The term $J_p$ related to the pressure is divided by $(dp^*/dz)^2$. The weighting coefficients are chosen arbitrarily. Fig. 11 shows the image of $J_{c+v,p}$ obtained by Eq. (22). A global minimum can be observed in Fig. 11.

**Table 3**
History of the virtual characterization by inverse method (conjugate gradient) with $K = 5000$ Pa.s$^n$ and $n = 0.5$ as initial point and a constant flowrate at 30 cc.s$^{-1}$.

| Iteration | $K$ (Pa.s$^n$) | $n$ | $J_{c+v,p}$ |
|---|---|---|---|
| 0 | 5000.00 | 0.5000 | 1.81E-01 |
| 1 | 4872.46 | 0.3857 | 1.26E-02 |
| 2 | 4821.55 | 0.3317 | 2.36E-04 |
| 3 | 4810.70 | 0.3278 | 1.74E-04 |
| 4 | 4642.36 | 0.3321 | 5.05E-07 |
| 5 | 4641.69 | 0.3319 | 1.14E-07 |
| 6 | 4639.97 | 0.3319 | 2.84E-08 |
| 7 | 4636.28 | 0.3320 | 3.28E-09 |

### 4.1. Inverse method demonstration with the cost function $J_{c+v,p}$

With a constant flowrate at 30 cc.s$^{-1}$, a virtual characterization by inverse method is carried out on a cost function described by Eq. (22). The Polak-Ribière's version of the conjugate gradient algorithm [35] coupled with the strong Wolfe criteria [36,37] is chosen. The Polak–Ribière version makes it convenient to restart the conjugate direction calculation [38], when the gradient residuals of two consecutive iterations are far enough from being orthogonal. The numerical gradient is computed in the $\ln(K) - n$ space. The material to be characterized is Polypropylene with $K = 4636$ Pa.s$^n$ and $n = 0.332$. The initial point (starting point) of the inverse method is chosen for $K = 5000$ Pa.s$^n$ and $n = 0.5$. The result and the iterations of the virtual characterization are presented in Fig. 12 and table 3.

**Table 4**
Virtual characterizations by inverse method (conjugate gradient) with different initial points of *K*-*n* and a constant flowrate at 30 cc.s−1.

| ***K*** initial (Pa.s$^n$) | ***n*** initial | Iteration number | ***K*** final (Pa.s$^n$) | ***n*** final | $J_{c+v,p}$ | Pressure loss prediction error |
|---|---|---|---|---|---|---|
| 5000 | 0.50 | 7 | 4636.28 | 0.3320 | 3.28E-09 | 0.005% |
| 5000 | 0.20 | 6 | 4634.85 | 0.3321 | 8.30E-09 | 0.013% |
| 2000 | 0.50 | 12 | 4636.70 | 0.3321 | 2.33E-08 | 0.038% |
| 2000 | 0.20 | 12 | 4634.38 | 0.3321 | 1.51E-08 | 0.022% |
| 8000 | 0.35 | 7 | 4635.23 | 0.3321 | 6.09E-09 | 0.011% |

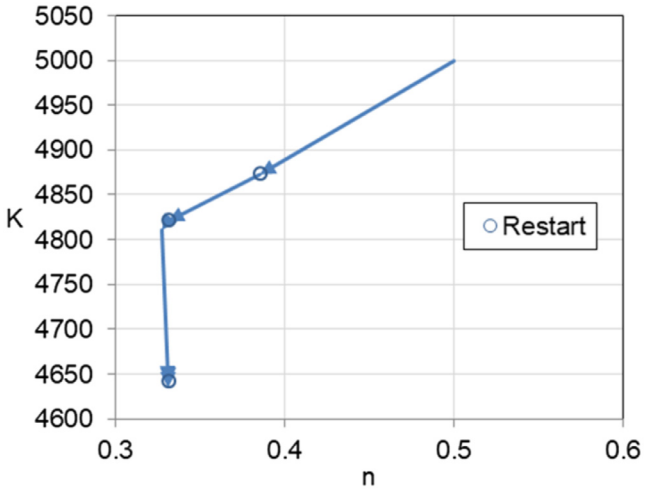


**Fig. 12.** History (path) of the virtual characterization by inverse method (conjugate gradient) with $K = 5000$ Pa.s$^n$ and $n = 0.5$ as initial point and a constant flowrate at 30 cc.s$^{-1}$.

The algorithm stops when the step size of the seventh iteration is less than a criterion (0.1 on the parameter $K$ and 0.0001 on the parameter $n$). Since the step size of each iteration is estimated numerically with an inevitable numerical error, the virtual characterization finds $K = 4636.28$ Pa.s$^n$ and $n = 0.332$ instead of $K = 4636$ Pa.s$^n$ and $n = 0.332$. When using the identified parameters $K$ and $n$ in the cylindrical or annular model (Eq. (20)), this 0.005% error on $K$ leads to a 0.005% error on the pressure loss prediction.

In the next part, several initial points of *K*-*n* are tested to verify the robustness of our method. The results are shown in table 4 and in Fig. 13.

Due to the complexity of the cost function's surface, the efficiency of the conjugate gradient algorithm depends on the initial point. Despite the different initial points, the algorithm always arrives at *K*-*n* values close to those sought ($K = 4636$ Pa.s$^n$ and $n = 0.332$) after about ten iterations. The largest error on the pressure loss prediction in the same geometry using the results (identified parameters) of the virtual characterization is 0.0381% among the tests demonstrated.

With our numerical model, each iteration takes about 40 minutes to compute five simulations for the gradient estimation (central differences). One possible improvement is to replace our numerical model by a reduced order model [39–41], which takes less than 0.1 second per iteration.

### *4.2. Error analysis of the demonstrated method with the cost function $J_{c+v,p}$*

An error study is carried out by introducing a « pressure measurement uncertainty ». The reference pressure (for $K = 4636$ Pa.s$^n$ and $n = 0.332$) is increased by 15%. With the same initial points, the characterization results are presented in table 5.

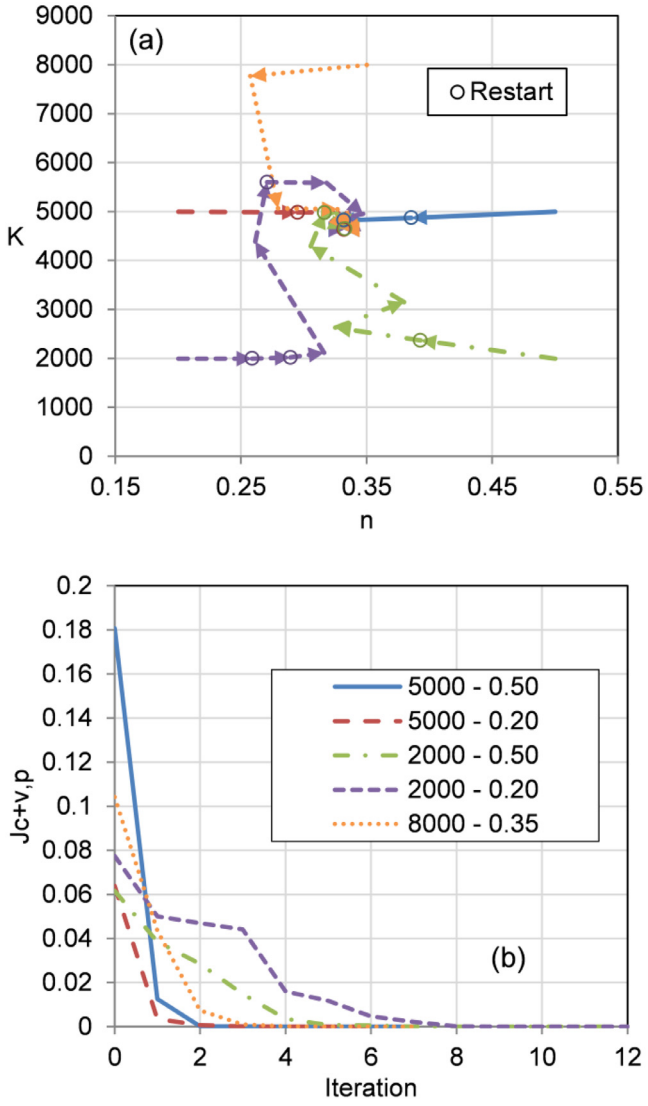


**Fig. 13.** (a) Paths of the virtual characterizations and (b) history of $J_{c+v,p}$ with different initial points of *K*-*n* and a constant flowrate at 30 cc.s$^{-1}$.

With the « measurement uncertainty », the characterizations take nearly the same numbers of iteration to arrive to the final solution. Table 5 shows that the final values of $K$ and $n$ are increased because of the increased pressure measurement. The errors in pressure loss prediction in the same geometry using the identified parameters are slightly less than 15%, which is reasonable with 15% of pressure measurement uncertainty in the weighted cost function (22). As the results in table 4, the final values of $J_{c+v,p}$ and the identified parameters *K*-*n* in table 5 vary little depending on the initial points, which shows again the method's robustness to different initial points.

**Table 5**
Virtual characterizations by inverse method (conjugate gradient) including an « artificial pressure measurement uncertainty » with different initial points of *K*-*n* and a constant flowrate at 30 cc.s$^{-1}$.

| ***K*** initial (Pa.s$^n$) | ***n*** initial | Iteration number | ***K*** final (Pa.s$^n$) | ***n*** final | $J_{c+v,p}$ | Pressure loss prediction error |
|---|---|---|---|---|---|---|
| 5000 | 0.50 | 4 | 4882.27 | 0.3498 | 7.22E-05 | 14.36% |
| 5000 | 0.20 | 8 | 4881.26 | 0.3499 | 7.22E-05 | 14.35% |
| 2000 | 0.50 | 10 | 4882.63 | 0.3498 | 7.23E-05 | 14.38% |
| 2000 | 0.20 | 9 | 4885.04 | 0.3498 | 7.23E-05 | 14.40% |
| 8000 | 0.35 | 7 | 4882.56 | 0.3498 | 7.21E-05 | 14.34% |

**Table 6**
Virtual characterizations by inverse method (conjugate gradient) including « artificial thermal measurement uncertainties» with different initial points of *K*-*n* and a constant flowrate at 30 cc.s$^{-1}$.

| ***K*** initial (Pa.s$^n$) | ***n*** initial | Iteration number | ***K*** final (Pa.s$^n$) | ***n*** final | $J_{c+v,p}$ | Pressure loss prediction error |
|---|---|---|---|---|---|---|
| 5000 | 0.50 | 3 | 4589.79 | 0.3308 | 1.089E-01 | -1.56% |
| 5000 | 0.20 | 4 | 4527.30 | 0.3401 | 1.085E-01 | 1.38% |
| 2000 | 0.50 | 5 | 4536.07 | 0.3429 | 1.086E-01 | 2.92% |
| 2000 | 0.20 | 10 | 4410.23 | 0.3445 | 1.084E-01 | 0.78% |
| 8000 | 0.35 | 5 | 4434.43 | 0.3442 | 1.085E-01 | 1.19% |

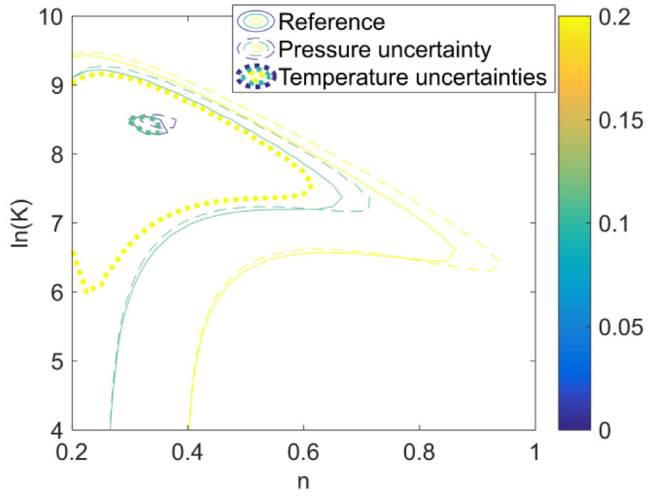


**Fig. 14.** Variation of the cost function $J_{c+v,p}$ due to 15% of increase on pressure measurement and uncertainties in temperature measurements (following a centered normal distribution with a standard deviation of 0.3 K) of Polypropylene with $K$= 4636 Pa.s$^n$ and $n$ = 0.332.

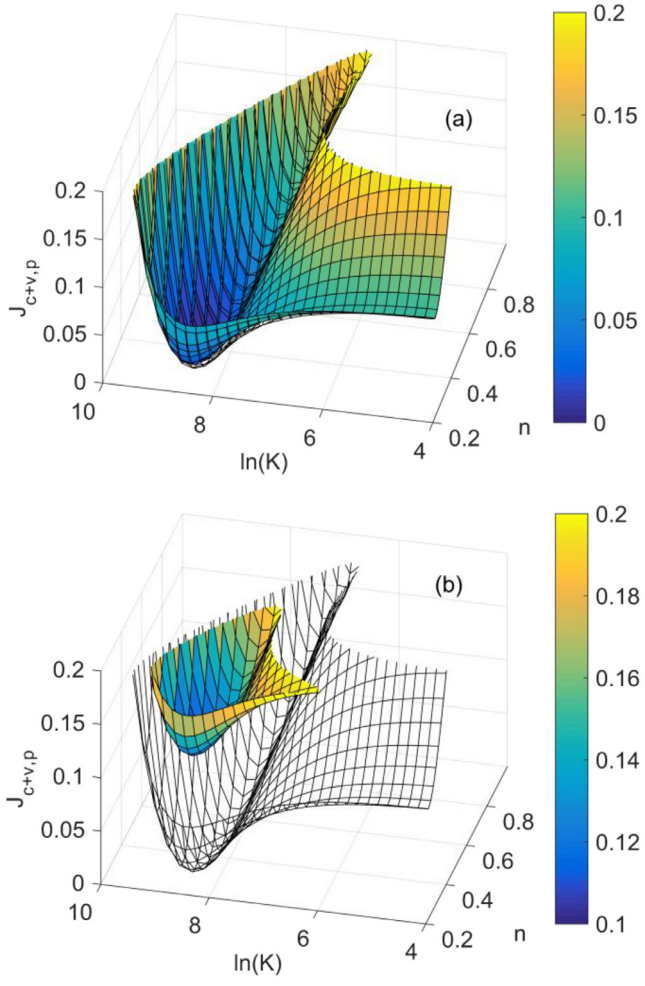


**Fig. 15.** 3D view of the variation of the cost function $J_{c+v,p}$ due to (a) 15% of increase on pressure measurement and (b) uncertainties in temperature measurements (following a centered normal distribution with a standard deviation of 0.3 K) of Polypropylene with $K$= 4636 Pa.s$^n$ and $n$ = 0.332.

Without any « pressure measurement uncertainty », another parallel part of the error study is brought off by adding « temperature measurement uncertainties » to the reference temperature data (for $K$ = 4636 Pa.s$^n$ and $n$ = 0.332). The « temperature measurement uncertainties » is created by using a centered normal distribution with a standard deviation of 0.3 K. The characterization results are presented in table 6.

We stop the algorithm when the value of $J_{c+v,p}$ drops below 0.1089, which is the residual error on the target ($K$ = 4636 Pa.s$^n$ and $n$ = 0.332) in our case. In fact, the uncertainties in thermal measurements bring out a residual error so that $J_{c+v,p}$ can't be improved within an area around the target. Once the algorithm steps into this area, there is no point in continuing the inverse characterization. In practice, the stopping criteria should be set according to the uncertainties' deviation. In table 6, the absolute values of the errors in the pressure loss prediction in the same geometry using the identified parameters are less than 3%. Compared to those in tables 4 and 5, the identified parameters *K*-*n* in table 6 vary more depending on the initial points due to the residual error. In terms of convergence speed, the starting point with low viscosity ($K$ = 2000 Pa.s$^n$ and $n$ = 0.2) requires the most iterations to reach the final solution. This starting point also takes the least efficient path in Fig. 13a.

To complete the error analysis, the variation of the cost function under the influence of the measurement uncertainties is illustrated

in Fig. 14. The reference $J_{c+v,p}$ of Polypropylene ($K = 4636$ Pa.s$^n$ and $n = 0.332$) without measurement uncertainty is presented in solid isovalue lines. $J_{c+v,p}$ with an increase of 15% on pressure measurement is presented in dashed isovalue lines. $J_{c+v,p}$ with uncertainties in temperature measurements, following a centered normal distribution with a standard deviation of 0.3 K, is presented in dotted isovalue lines. Three line colors represent the isovalues of 0.003, 0.112 and 0.2. We specify that the 0.003 isovalue line does not exist for the cost function with uncertainties in temperature measurements.

The reference $J_{c+v,p}$ in Fig. 14 is similar to the one in Fig 11, with a confluence of the « vertical valley of convection » and the « inclined valley of pressure measurement ». The increase of 15% on pressure measurement shifts the « inclined valley » towards the top/right side of the figure. The dashed contour with an isovalue of 0.003 is clearly shifted towards the top/right side by the « pressure measurement uncertainty ». As for uncertainties in temperature measurements, although a residual error is induced by the uncertainties following a centered normal distribution, the dotted contour having an isovalue of 0.112 stays close to the reference solid contour with an isovalue of 0.003. The 3D surfaces of the cost functions in Fig. 14 are shown in Fig. 15 ((a) for « pressure measurement uncertainty » and (b) for « temperature measurement uncertainties »), with the reference surface being transparent.

Fig. 15a confirms the slight deformation of the cost function surface due to the uncertainty in pressure measurement. The deformation is constrained by the « vertical valley of convection », which almost stays still when the values of $\ln(K)$ and $n$ are close to 4 and 0.2. In Fig. 15b, the uncertainties in temperature measurements following a centered normal distribution flatten the minimum valleys and create a residual error. No local minimum is observed with the presence of uncertainties.

## 5. Conclusion

In the first section, a non-isothermal annular flow model is presented. The polymer flow with a large Graetz number isolates the central axis from external thermal disturbances due to the environment. In addition, an analytical expression proclaims that the annular geometry promotes viscous dissipation on the central axis' surface more than any other area in the flow. Some numerical analysis is thus carried out to study the thermo-rheological phenomena measured by the virtual thermocouples on the central axis.

By analyzing the viscous heating via the temperature measurements on the central axis during one injection at a constant flowrate, one critical point $(\dot{\bar{\gamma}}_c, \eta_c)$ can be identified on the viscosity curve. More critical points can be obtained by modulating the flowrate. Although the point cloud is obtained with the power-law model, it is possible to draw a curve from the point cloud without using any existing model.

The heat convection between the flow and the central axis can be promoted when the flow comes in with a temperature different from the initial temperature of the axis. This phenomenon is sensitive to the power-law parameter $n$ and insensitive to the other parameter $K$. For a viscous material which induces an important viscous heating, it is possible to differentiate two injections with two different inlet temperatures or with two different initial temperature fields of the central axis, to erase the influence of viscous heating. In this paper, we call this strategy: differential convection characterization. The differential convection characterization with different initial temperature fields of the central axis can be performed without the need of knowing precisely the inlet temperature profiles as long as they are the same during those two injections. An alternative solution is to assign a heat source to the central axis. The differential convection characterization based on the different heating power at the central axis is also unsusceptible to the inlet temperature's non-homogeneous profile. It should be noted that if the viscous heating is not over dominant compared to the heat convection, one injection is enough to look into the heat convection phenomenon.

The pressure loss depends linearly on the power-law parameter $K$, which makes it possible to use this measurement with the heat convection analysis to identify a whole power law. However, the pressure loss gives nearly the same information as the viscous dissipation. We can use the heat convection analysis with either the viscous heating analysis or the pressure loss measurement to achieve the identification with a consistent flowrate.

In the last section of the paper, an example of weighted cost function is given for a fictive material and shows a unique minimum within the viscosity range of our study. With the power-law parameters of Polypropylene, a virtual inverse characterization is exemplified and proved to have a satisfying theoretical precision and robustness. An error analysis is also carried out by taking measurement uncertainties into account. No major threat to the stability of the exemplified method is observed. Despite this, an experimental device should be built to further verify the mentioned methods in real application.

On a polymer production line, the inlet temperature profile can be repeatable but not precisely controlled. The flowrate is often fixed to ensure a production cadence. With the strategies presented in this paper, an annular device can be suitable for in-line monitoring. For example, this device can be integrated to a production line as part of the injection nozzle and use every two injection cycles to accomplish a differential convection characterization. The injection pressure can be adjusted according to the estimated viscosity to ensure the filling of the mold and be optimal in terms of energy consumption.

With a numerical model, the calculation time could be long, but it is improvable with, for example, a reduced order model.

## Declaration of Competing Interest

The authors declare that they have no known competing financial interests or personal relationships that could have appeared to influence the work reported in this paper.

## CRediT authorship contribution statement

**Qiao Lin:** Writing – original draft, Methodology, Software, Investigation. **Nadine Allanic:** Writing – review & editing, Conceptualization, Project administration. **Rémi Deterre:** Writing – review & editing, Conceptualization, Formal analysis. **Pierre Mousseau:** Conceptualization, Supervision. **Manuel Girault:** Writing – review & editing, Software.

## Acknowledgement

This work was supported by the French Ministry of Higher Education, Research and Innovation and held in the GEPEA Laboratory (IUT Nantes).

## Supplementary materials

Supplementary material associated with this article can be found, in the online version, at doi:10.1016/j.ijheatmasstransfer.2021.121988.

## References

[1] F. Trochu, E. Ruiz, V. Achim, S. Soukane, Advanced numerical simulation of liquid composite molding for process analysis and optimization, Compos. Part Appl. Sci. Manuf. 37 (2006) 890–902, doi:10.1016/j.compositesa.2005.06.003.

[2] D.E. Smith, Design sensitivity analysis and optimization for polymer sheet extrusion and mold filling processes, Int. J. Numer. Methods Eng. 57 (2003) 1381–1411.
[3] J.-Y. Chen, K.-J. Yang, M.-S. Huang, Online quality monitoring of molten resin in injection molding, Int. J. Heat Mass Transf. 122 (2018) 681–693, doi:10.1016/j.ijheatmasstransfer.2018.02.019.
[4] E. Ojogbo, E.O. Ogunsona, T.H. Mekonnen, Chemical and physical modifications of starch for renewable polymeric materials, Mater. Today Sustain 7 (8) (2020) 100028, doi:10.1016/j.mtsust.2019.100028.
[5] G.E.H. Sleiman, I. Petit, N. Allanic, S. Belhabib, Y. Madec, J. Launay, R. Deterre, Study of the rheological behavior of polypropylene/polyethylene extruded mixture using an instrumented die, AIP Conf. Proc. (2017) 040005 1914, doi:10.1063/1.5016715.
[6] J.M. Dealy, T.O. Broadhead, Process rheometers for molten plastics: A survey of existing technology, Polym. Eng. Sci. 33 (1993) 1513–1523, doi:10.1002/pen.760332302.
[7] J. Aho, S. Syrjälä, Shear viscosity measurements of polymer melts using injection molding machine with adjustable slit die, Polym. Test. 30 (2011) 595–601, doi:10.1016/j.polymertesting.2011.04.014.
[8] N. Zhang, M.D. Gilchrist, Characterization of thermo-rheological behavior of polymer melts during the micro injection moulding process, Polym. Test. 31 (2012) 748–758, doi:10.1016/j.polymertesting.2012.04.012.
[9] A. Fernandez, M. Muniesa, C. Javierre, In-line rheological testing of thermoplastics and a monitored device for an injection moulding machine: Application to raw and recycled polypropylene, Polym. Test. 33 (2014) 107–115, doi:10.1016/j.polymertesting.2013.11.008.
[10] V. Mazzanti, F. Mollica, In-line rheometry of polypropylene based Wood Polymer Composites, Polym. Test. 47 (2015) 30–35, doi:10.1016/j.polymertesting.2015.08.003.
[11] H.-J. Luger, J. Miethlinger, Development of an online rheometer for simultaneous measurement of shear and extensional viscosity during the polymer extrusion process, Polym. Test. 77 (2019) 105914, doi:10.1016/j.polymertesting.2019.105914.
[12] W. Ostwald, About the rate function of the viscosity of dispersed systems, Kolloid Z 36 (1925) 99–117.
[13] A. Waele, Viscometry and plastometry, Oil Colour Chem. Assoc. 6 (1923) 33–88.
[14] A. Gottfert, Real-time viscosity control with capillary rheometry, Kunststoffe Ger. Plast. 76 (1986) 1200–1203.
[15] M. Karkri, Y. Jarny, P. Mousseau, Thermal state of an incompressible pseudo-plastic fluid and Nusselt number at the interface fluid–die wall, Int. J. Therm. Sci. 47 (2008) 1284–1293, doi:10.1016/j.ijthermalsci.2007.11.009.
[16] C. Pujos, Estimation de la rhéologie d'un polymère dans une filière d'extrusion - Simulation d'écoulement avec transferts thermiques et inversion de mesures, These de doctorat, Bordeaux 1 (2006).
[17] C. Pujos, N. Régnier, G. Defaye, Determination of the inlet temperature profile of an extrusion die in unsteady flow, Chem. Eng. Process. Process Intensif. 47 (2008) 456–462, doi:10.1016/j.cep.2007.01.008.
[18] Y. Wielhorski, P. Mousseau, Y. Jarny, D. Delaunay, N. Lefevre, Thermal balance between viscous heating and inlet thermal condition in non stationary polymer flow through a cylindrical die, Int. J. Therm. Sci. 50 (2011) 769–778, doi:10.1016/j.ijthermalsci.2010.12.003.
[19] J. Launay, N. Allanic, P. Mousseau, R. Deterre, C. Plot, Effect of viscous dissipation in the prediction of thermal behavior of an elastomer cylindrical flow, J. Mater. Process. Technol. 252 (2018) 680–687, doi:10.1016/j.jmatprotec.2017.10.035.
[20] N. Allanic, R. Deterre, P. Mousseau, D. Couedel, in: Thermal behavior of a concentric annular polymer flow, AIP Publishing LLC, 2019, p. 130004. AIP Conf. Proc..
[21] J.-F. Agassant, P. Avenas, P.J. Carreau, B. Vergnes, M. Vincent, Polymer processing: principles and modeling, Carl Hanser Verlag GmbH Co KG, 2017.
[22] R.B. Bird, Experimental tests of generalised newtonian models containing a zero-shear viscosity and a characteristic time, Can. J. Chem. Eng. 43 (1965) 161–168, doi:10.1002/cjce.5450430402.
[23] D.W. McEachern, Axial laminar flow of a non-Newtonian fluid in an annulus, AIChE J 12 (1966) 328–332.
[24] D.K. Gartling, E.B. Becker, Finite element analysis of viscous, incompressible fluid flow: Part 1 : Basic methodology, Comput. Methods Appl. Mech. Eng. 8 (1976) 51–60, doi:10.1016/0045-7825(76)90052-9.
[25] J. Crank, P. Nicolson, A practical method for numerical evaluation of solutions of partial differential equations of the heat-conduction type, Math. Proc. Camb. Philos. Soc. 43 (1947) 50–67, doi:10.1017/S0305004100023197.
[26] R. Deterre, F. Nicoleau, Q. Lin, N. Allanic, P. Mousseau, The flow of power-law fluids in concentric annuli: A full analytical approximate solution, J. Non-Newton. Fluid Mech. 285 (2020) 104392, doi:10.1016/j.jnnfm.2020.104392.
[27] K. Pearson, F. Galton VII, Note on regression and inheritance in the case of two parents, Proc. R. Soc. Lond. 58 (1895) 240–242, doi:10.1098/rspl.1895.0041.
[28] X. Hernot, C. Moussa, O. Bartier, Study of the concept of representative strain and constraint factor introduced by Vickers indentation, Mech. Mater. 68 (2014) 1–14, doi:10.1016/j.mechmat.2013.07.004.
[29] V. Hristov, E. Takacs, J. Vlachopoulos, Surface tearing and wall slip phenomena in extrusion of highly filled HDPE/wood flour composites, Polym. Eng. Sci. 46 (2006) 1204–1214.
[30] C. Moussa, X. Hernot, O. Bartier, G. Delattre, G. Mauvoisin, Evaluation of the tensile properties of a material through spherical indentation: definition of an average representative strain and a confidence domain, J. Mater. Sci. 49 (2014) 592–603, doi:10.1007/s10853-013-7739-1.
[31] C. Abeykoon, A.L. Kelly, E.C. Brown, P.D. Coates, The effect of materials, process settings and screw geometry on energy consumption and melt temperature in single screw extrusion, Appl. Energy. 180 (2016) 880–894, doi:10.1016/j.apenergy.2016.07.014.
[32] G. El Hajj Sleiman, Aptitude à la mise en oeuvre de thermoplastiques recyclés et de biopolymère : analyse thermorhéologique de mélanges PP/PE, These de doctorat, Nantes (2018) http://www.theses.fr/2018NANT4029. accessed April 27, 2021.
[33] R.W. Hanks, K.M. Larsen, The flow of power-law non-Newtonian fluids in concentric annuli, Ind. Eng. Chem. Fundam. 18 (1979) 33–35.
[34] B. Rabinowitsch, Über die viskosität und elastizität von solen, Z. Für Phys. Chem. 145 (1929) 1–26.
[35] E. Polak, G. Ribiere, Note sur la convergence de méthodes de directions conjuguées, Rev. Fr. Inform. Rech. Opérationnelle Sér. Rouge. 3 (1969) 35–43, doi:10.1051/m2an/196903R100351.
[36] P. Wolfe, Convergence conditions for ascent methods, SIAM Rev 11 (1969) 226–235.
[37] P. Wolfe, Convergence conditions for ascent methods, II: Some corrections, SIAM Rev. 13 (1971) 185–188.
[38] J.R. Shewchuk, An introduction to the conjugate gradient method without the agonizing pain, Carnegie-Mellon University. Department of Computer Science, 1994.
[39] M. Girault, J. Launay, N. Allanic, P. Mousseau, R. Deterre, Development of a thermal Reduced Order Model with explicit dependence on viscosity for a generalized Newtonian fluid, J. Non-Newton. Fluid Mech. 260 (2018) 26–39.
[40] M. Girault, D. Petit, Identification methods in nonlinear heat conduction. Part I: Model reduction, Int. J. Heat Mass Transf. 48 (2005) 105–118, doi:10.1016/j.ijheatmasstransfer.2004.06.032.
[41] M. Girault, D. Petit, Identification methods in nonlinear heat conduction. Part II: inverse problem using a reduced model, Int. J. Heat Mass Transf. 48 (2005) 119–133, doi:10.1016/j.ijheatmasstransfer.2004.06.033.